

High-resolution spatial reconstruction of cellular force-generating domains using physical constraints and L^1 regularization

Joshua C. Chang, Yanli Liu, and Tom Chou

*Epidemiology and Biostatistics Section, Rehabilitation Medicine,
Clinical Center, The National Institutes of Health, Bethesda MD, 20892 and
Depts. of Biomathematics and Mathematics, UCLA, Los Angeles, CA 90095-1766*

We develop a method to reconstruct, from measured displacements of the underlying elastic substrate, the spatially dependent forces that cells or tissues impart on it. Given newly available high-resolution methods to image substrate displacements, it is desirable to be able to reconstruct small scale, compactly supported focal adhesions, which are localized and can exist only within the footprint of the cell or tissue. We solve this inverse problem using methods of L^1 optimization often used in image segmentation. In addition to the standard quadratic data mismatch terms that defines least-squares fitting, we motivate a term in the objective function which penalizes variations in the tensor invariants of the reconstructed stress while preserving boundaries. By minimizing the objective function subject to appropriate physical constraints, we are able to efficiently reconstruct stress fields with localized structure from simulated and experimental substrate displacements. We provide a numerical method for setting up a discretized inverse problem that is solvable by standard convex optimization techniques. Our method incorporates the exact solution for the stress tensor accurate to first-order finite-differences, motivates the use of distance-based cutoffs for data inclusion, and finds—under loose regularity conditions—the reconstruction error that results.

INTRODUCTION

The adhesion of cells and tissues to their environment has profound consequences on processes such as cell polarization [1], division, differentiation [2], tissue morphology during development [3], wound healing [4–6], and cancer metastasis [7]. Hence, quantifying how cells attach to an impart force on the surrounding material is an important technical challenge in cell biology.

Cell motility and response to signals have hitherto typically been studied in two-dimensional geometries in which cells are placed on a flat elastic substrate. Dynamic adhesion between the cells and the substrate are realized through *e.g.*, lamellapodia, filopodia, and dynamically reorganizing focal adhesions [8]. Such structures are spatially localized, as shown in Fig. 1. Similarly, on larger length scales, a collection of cells can give rise to localized stress distributions. For example, the leading edge of a cell layer produces the pulling force that leads to migration in wound healing assays.

Dynamically varying force-generating structures are often small and difficult to image, especially without biochemical modification such as incorporation of fluorescent dyes. Therefore, other methods for inferring their positions and magnitudes have been developed. Methods using deformation of pillar structures [9] or textured substrates have been developed [10]. These methods require the cell to attach to a nonflat interface. The simplest method compatible with a flat interface relies on measuring the displacement of fiduciary markers, such as gold nanoparticles, embedded in the elastic substrate [11]. The measured displacements are an indirect probe of the force-generating structures, *e.g.*, focal adhesions. Any inversion method should be able to not only reconstruct the

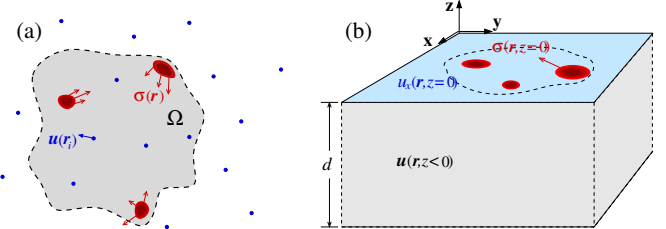


FIG. 1. A schematic of an isolated cell. (a) The boundary of the cell footprint is denoted by the dashed curve, the support of the stress field is represented by the red regions that impart a stress $\mathbf{F}(x, y)$ on the surface. Displacements $\mathbf{u}(\mathbf{r}_i)$ of the elastic medium are measured at position $\mathbf{r}_i = x_i\hat{x} + y_i\hat{y} + z_i\hat{z}$ (blue dots) that can be inside or outside the cell footprint, on the surface ($z_i = 0$), or below the surface ($z_i < 0$). (b). A perspective view of the elastic substrate and cellular footprint.

positions and magnitudes of the stress field, but should ideally be able to capture potentially sharp boundaries of the stress-generating structures. However, fiduciary markers embedded in the 3D substrate are typically too sparse to reveal a displacement field with sufficient resolution to infer small cellular focal adhesion structures. To image such subcellular stress structures, high resolution reconstructions are required [12]. Experimentally, a new high-resolution imaging method has been developed using 9 μm-period grid patterning of the substrate [13]. A surface grid pattern of fluorescent adhesion proteins allows surface deformation to be directly measured using conventional microscopes.

In light of such higher spatial resolution techniques, we develop a novel method for elastic stress source recovery

using ideas developed for image segmentation [14]. This class of methods relies on optimization that uses an L^1 regularization term in the objective function [15]. This type of regularization term is not derived from a fundamental physical law, but represents a prior knowledge that the function to be recovered is sparse in content except near edges. In addition, the overall objective function will be constructed to obey physical constraints and symmetries.

In the next section, we review the standard linear equations of elasticity that describe the displacement field as a function of an arbitrary surface stress distribution. This model is then used to construct the data mismatch term in the objective function. We then motivate regularization and constraint terms in the full objective function. Finally, we demonstrate our method using both simulated and experimental data. Our method provides good reconstruction of localized structures that exhibit desirable qualities such as the suppression of Gibbs ringing phenomenon at the boundaries of the stress structures.

ELASTIC MODEL

We first derive the linear elastic green's function associated with a point force applied to the surface of a semi-infinite half-space, as shown in Fig. 1(b). We assume that the elastic medium is infinite in both depth ($d \rightarrow \infty$) and lateral extent. The Green's function tensor defined in the domain $\mathcal{D} = \{(x, y, z) | x, y \in R, z \leq 0\}$ is given by

$$\mathbf{G} = \begin{bmatrix} G_{xx}(x, y, z) & G_{xy}(x, y, z) & G_{xz}(x, y, z) \\ G_{yx}(x, y, z) & G_{yy}(x, y, z) & G_{yz}(x, y, z) \\ G_{zx}(x, y, z) & G_{zy}(x, y, z) & G_{zz}(x, y, z) \end{bmatrix} \quad (1)$$

where the components are explicitly given in Appendix A. For example,

$$G_{sz,ss}(x, y, z) = \frac{1 + \nu}{2\pi E} \left(\frac{sz}{R_\perp^3} \pm \frac{(1 - 2\nu)s}{R_\perp(R_\perp - z)} \right). \quad (2)$$

where $s \equiv x, y$. The equation with \pm corresponds to G_{sz} and G_{zs} , respectively, and $R_\perp \equiv \sqrt{x^2 + y^2}$. The Young's modulus and Poisson ratio of the elastic substrate are denoted by E and ν , respectively. For Matrigel, $E \approx 4 \pm 3 \times 10^2$ Pa and $\nu \approx 0.5$ [16]. Throughout the rest of this manuscript, we will express stress in units of E .

The displacement of a material point at $(x, y, z \leq 0)$ in the medium due to a stress distribution \mathbf{F} is simply the convolution $\mathbf{u}(\mathbf{r}) \equiv [u_x \ u_y \ u_z]^\top = \mathbf{G} * \mathbf{F}$.

For our specific problem, we shall restrict the forces to surface stresses $\sigma_{x,y}$ that act on the plane perpendicular to the \hat{z} axis. We define the in-plane stress distribution, at depth z , as $\boldsymbol{\sigma}(x, y, z) = \sigma_{xz}(x, y, z)\hat{x} + \sigma_{yz}(x, y, z)\hat{y}$. The resulting surface-level displacement fields become

$$u_s(x, y) = \sum_{k=x, y} \int_{\Omega} dx' dy' G_{sk}(x - x', y - y') \sigma_{kz}(x', y') \quad (3)$$

where $G_{ij}(x, y) \equiv G_{ij}(x, y, z = 0)$ and $\sigma_{sz}(x, y) \equiv \sigma_{sz}(x, y, z = 0)$. Note that tangential stresses can lead to displacement in the normal direction.

INVERSE PROBLEM

Next, we develop an objective function for which the minimizing solution provides a good approximation to the underlying stress field, while preserving discontinuities. The first component is simply a quadratic data mismatch term defined by the sum over the displacements measured at the N measurement positions at \mathbf{r}_i :

$$\Phi_{\text{data}}[\boldsymbol{\sigma}] = \sum_i^N |\mathbf{u}^{\text{data}}(\mathbf{r}_i) - \mathbf{u}(\mathbf{r}_i)|^2. \quad (4)$$

Since $\mathbf{u}^{\text{data}}(\mathbf{r}_i)$ is given, and $\mathbf{u}(\mathbf{r}_i)$ is given by the linear model of Eq. 3, this contribution to the objective function is a functional over the surface-stress function $\boldsymbol{\sigma}(\mathbf{r}_\perp)$. For simplicity, we will assume that the data points are sampled over an uniform grid with coordinates given $\{(x_j, y_k) : j \in \{1, 2, \dots, J\}, k \in \{1, 2, \dots, K\}\}$.

In Eqs 3, we have restricted the domain of integration to lie within the cell footprint Ω , further emphasizing that $\boldsymbol{\sigma}$ has compact support. As a consequence of compact support, for a fixed, discretized approximation of σ_{xz}, σ_{yz} , the displacements can be obtained exactly by solving an equivalent system of linear equations of finite dimension.

Here we explicitly define this system of linear equations given a piecewise-affine approximation of the stress field. Let us consider the first-order approximation of σ_{xz} and σ_{yz} using central finite differences, for $x \in [x_j - \delta x/2, x_j + \delta x/2] \cap y \in [y_j - \delta y/2, y_j + \delta y/2]$,

$$\begin{aligned} \sigma_{xz}(x, y) = & \sigma_{xz}(x_i, y_j) \\ & + (x - x_i) \frac{\sigma_{xz}(x_{i+1}, y_j) - \sigma_{xz}(x_{i-1}, y_j)}{2\delta x} \\ & + (y - y_j) \frac{\sigma_{xz}(x_i, y_{j+1}) - \sigma_{xz}(x_i, y_{j-1})}{2\delta y} \\ & + \mathcal{O}(\delta x)^2 + \mathcal{O}(\delta y)^2, \end{aligned} \quad (5)$$

where i, j denotes a tuple of grid coordinates. In effect, we are performing sub-pixel interpolation of the stress where the stress is fully-determined by its values at the grid vertices.

Upon using Eq. 5, we can rewrite Eq. 3 by decomposing the integral into a sum of integrals over grid cells.

After further regrouping terms, we find a linear system of equations for u_x at all grid points simultaneously,

$$u_x(x_n, y_m) = X^{nmjk} \sigma_{xz}(x_j, y_k) + Y^{nmjk} \sigma_{yz}(x_j, y_k), \quad (6)$$

where the tensors X^{nmjk} and Y^{nmjk} are given in Appendix B and summation notation for each index tuple (j, k) has been implicitly assumed.

From an equation-counting perspective, the system of equations is exactly determined given that one has at least as many measurement points as grid cells in the resolution that one wishes to reconstruct the stress field, provided that one is able to measure displacements in both principle directions. Even if one is able to measure both displacements, the problem may still be difficult since the inversion of Eq. 6 maybe highly ill-conditioned and the measurements are taken in the presence of noise at a finite precision. To resolve these issues, we introduce a number of physically consistent constraints and regularization terms relevant to this system.

Physical regularization

To better condition the inference of $\boldsymbol{\sigma}(x, y)$, we regularize this problem by forcing the reconstruction to obey some physically relevant characteristics of the surface stress. First, since we are assuming inertial effects are negligible, we require that the net force is zero, or that

$$\int_{\Omega} \sigma_{xz}(x, y) dx dy = \int_{\Omega} \sigma_{yz}(x, y) dx dy = 0. \quad (7)$$

Likewise, we require that there is no net torque, or that

$$\int_{\Omega} x \sigma_{yz}(x, y) dx dy = \int_{\Omega} y \sigma_{xz}(x, y) dx dy. \quad (8)$$

Finally, we would like to impose regularity on the reconstructed fields while preserving both rotational invariance and the sharp stress boundaries. To this end we employ a variant of a penalty used often in image processing applications, where we wish to penalize the L^1 norm of the variation in the fields, or the total variation. To do this in a manner that is consistent with the philosophy that rotation of the data should not affect the result, we penalize the total variation norm of the invariants of the stress tensor. In the case of two-dimensional tensors, of which the surface stress is an example, the tensor invariants are the trace

$$\text{Tr}(\boldsymbol{\sigma}) = \sigma_{xz} + \sigma_{yz} \quad (9)$$

and the determinant

$$\text{Det}(\boldsymbol{\sigma}) = \sigma_{xz} \sigma_{yz}. \quad (10)$$

Any regularization penalty imposed on the reconstruction problem must be a functional of these invariants in

order to maintain rotational invariance relative to the choice of observation frame of the reconstructed stress tensor.

Since there are no physical principles or symmetries to exploit beyond using the trace and determinant, there is some choice in the form of the the regularization term Φ_{reg} . In this manuscript, we will restrict ourselves to regularizers that are functions of the trace of the stress tensor. In particular, we are interested in the L^1 norm of the trace

$$\Phi_{L^1(\text{Tr})} = \int_{\Omega} |\sigma_{xz}(x, y) + \sigma_{yz}(x, y)| dx dy \quad (11)$$

and total variation norm of the trace

$$\Phi_{\text{TV}(\text{Tr})} = \int_{\Omega} |\nabla(\sigma_{xz}(x, y) + \sigma_{yz}(x, y))| dx dy. \quad (12)$$

Using either of these expressions as the regularization norm Φ_{reg} suggests the penalized optimization problem

$$\hat{\boldsymbol{\sigma}} | \lambda = \arg \min_{\boldsymbol{\sigma}} \{ \Phi_{\text{data}}[\boldsymbol{\sigma}] + \lambda \Phi_{\text{reg}}[\boldsymbol{\sigma}] \}, \quad (13)$$

subject to the no-force and no-torque constraints (Eqs. 7 and 8) mentioned above, where $\lambda > 0$ is a tunable parameter. This problem is in a standard form that is directly solvable using a variety of optimization routines. In our implementation, we use a second-order quadratic cone solver [17].

To reduce the size of the system of equations described in Eqs. 6, we note that the Green's function falls off at a rate of $|\mathbf{r}|^{-1}$. However, when combined with the zero-force constraint, the relationship between the displacements and the support of the stress field falls off at the much quicker rate of $|\mathbf{r}|^{-2}$. Formally, if $\Omega = \text{sup}(\boldsymbol{\sigma}) \subset \mathbb{R}^2$ is compact, and $\int \boldsymbol{\sigma}(\mathbf{r}) d\mathbf{r} = \mathbf{0}$, then as $\mathbf{r} \rightarrow \infty$, $u_{x,y}(\mathbf{r}) = \mathcal{O}(|\mathbf{r}|^{-2})$.

The decay of the influence of stress on the system provides justification for setting distance-based cut-offs of the linear system. The effect of the cut-off is to limit the left-hand side of Eq. 6 to locations only within some maximal distance R from the outline of the cell.

RESULTS

We implemented our regularized inversion method in Python version 3.5, where optimization is performed using the cvxpy package with the ecos solver. Our implementation is available at <https://github.com/joshchang/tractionforce>.

First we tested our method on simulated data derived from the two different force- and torque-free test stress fields shown in Fig. 2. The first test stress field we consider is

$$\sigma_{rz}(r, \theta) = f_r \sin(m\theta), \quad \sigma_{\theta z}(r, \theta) = f_\theta \cos(n\theta), \quad (14)$$

for $a < r < 1$, and zero otherwise. Here, m, n are integers and if we normalize the stresses by the Young's modulus E , f_r and f_θ are constants.

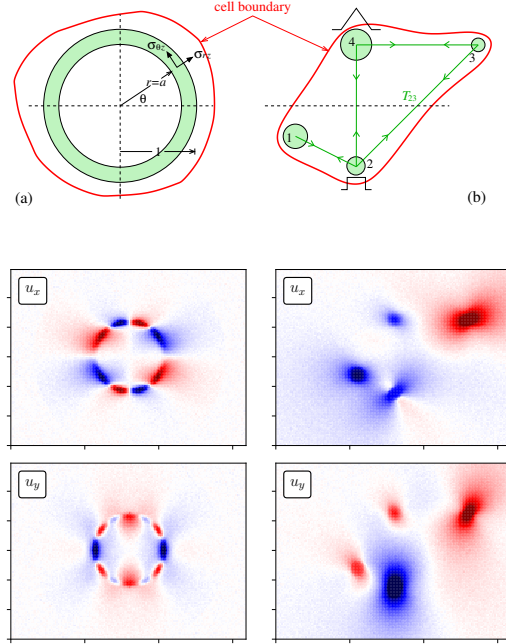


FIG. 2. Test stress fields and surface displacements. (a) An annular stress distribution of forces in the θ and r directions. (b) Four focal adhesions under mutual tension represented by the green lines representing filaments. The red borders represent the extent of the cell footprint and can be determined experimentally as part of the imaging. Mathematically, the cell boundary forms the basis for a constraint on the stress distribution and we explore the dependence of the quality of reconstruction on the footprint constraint. (c) and (d) show the surface displacement field associated with the stress distributions in (a) and (b), respectively.

The second stress field we test consists of four separated circular stress pads, or focal adhesions, with radii $r_1 = 1/5$, $r_2 = 1/6$, $r_3 = 1/8$, and $r_4 = 1/4$, and centers at positions $(x_1, y_1) = (-1, -1/2)$, $(x_2, y_2) = (0, -1)$, $(x_3, y_3) = (2, 1)$, and $(x_4, y_4) = (0, 1)$. The pads 2,3, and 4 are connected in a triangle as shown, while pad 1 is connected only to pad 2. The tensions along these connections give rise to surface stresses imparted by the pads onto the substrate. We will assume that the stress fields in pads 1,2, and 3 are uniformly distributed within the circular disks. For pad 4, we assume that the filaments connected to it distributed according to a cone-like density function. Thus, the stress field within pad 4 linearly decrease along the radial direction. The stresses $\boldsymbol{\sigma}^{(i)}$ un-

FIG. 3. Inversion results for test stress fields. (a) Inversion for the annular stress field with $m = 3$, $n = 5$ and ...using different cell boundaries....

der each patch i are decomposed into contributions arising from the total tension T_{ij} connecting them with pad j and can be expressed in the form

$$\boldsymbol{\sigma}^{(1)} = a_{12} \left(\hat{x} - \frac{\hat{y}}{2} \right) \quad (15)$$

$$\boldsymbol{\sigma}^{(2)} = \frac{G_4}{A_2} \hat{y} - a_{12} \frac{A_1}{A_2} \left(\hat{x} - \frac{\hat{y}}{2} \right) + a_{23} (\hat{x} + \hat{y}) \quad (16)$$

$$\boldsymbol{\sigma}^{(3)} = -\hat{x} \frac{G_4}{A_3} - a_{23} \frac{A_2}{A_3} (\hat{x} + \hat{y}) \quad (17)$$

$$\boldsymbol{\sigma}^{(4)} = g_4 \left(1 - \frac{r}{r_4} \right) (\hat{x} - \hat{y}) \quad (18)$$

where $a_{12}, a_{23}, g_4 > 0$ are constant amplitudes, $A_i = \pi r_i^2$ are the pad areas, and

$$G_4 = g_4 \int_0^{r_4} \left(1 - \frac{r}{r_4} \right) dr = \frac{g_4 \pi r_4^2}{3} \quad (19)$$

is the total force on pad 4 in each direction. Note that both test stress fields are constructed to be force- and torque-free. We first generate the displacement fields using the Green's function (*i.e.*, Eq. 3 for surface values $\mathbf{u}(x, y, z = 0)$) and then recover $\boldsymbol{\sigma}(\mathbf{r})$ from these displacements.

DO SOME RECONSTRUCTIONS FOR DIFFERENT REGULARIZATIONS, FOOTPRINTS, AND GRID RESOLUTIONS

We also compared reconstruction of the surface stress using our rotationally invariant norms of Eq. 11 and Eq. 12 against alternate isotropic norms. As an alternative to the L^1 norm on the trace we compared

$$\Phi_{L1} = \int_{\Omega} |\sigma_{xz}(x, y) + \sigma_{yz}(x, y)| dr, \quad (20)$$

and as alternatives to the total variation on the trace we looked at

$$\Phi_{TV_1} = \int_{\Omega} (|\nabla \sigma_{xz}(x, y)| + |\nabla \sigma_{yz}(x, y)|) dr \quad (21)$$

and

$$\Phi_{TV_2} = \int_{\Omega} (|\partial_x \sigma_{xz}| + |\partial_y \sigma_{xz}| + |\partial_x \sigma_{yz}| + |\partial_y \sigma_{yz}|) dr. \quad (22)$$

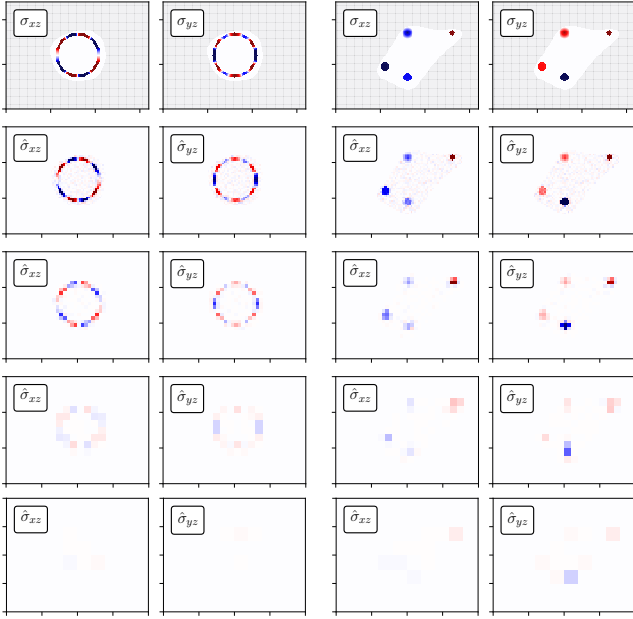


FIG. 4. **Grid coarsening** Using every 2^n lattice points of observations.

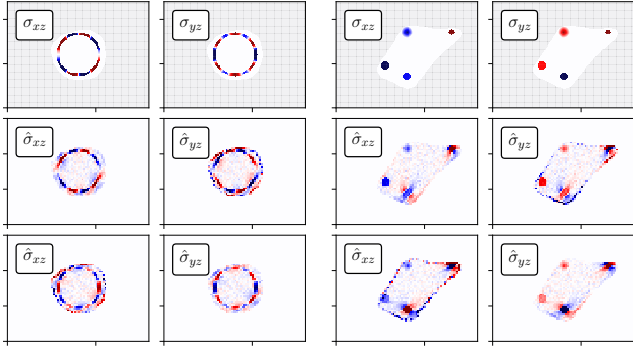


FIG. 5. **Unidirectional displacement measurements**
Sets of reconstructions using displacements under only \hat{x} or \hat{y} directions

The adjustable parameter λ was chosen in each instance by examining the balance between data mismatch and regularity using trade-off curves shown in Fig. 9, and taking the value for λ that yields a point farthest away from the line segment joining the ends of the plot. In Fig. 9, the chosen value of λ corresponds to the given balance between regularity and data fidelity marked by the red circle. The solution corresponding to this particular value of λ is shown in the middle column on the right. For reference, under-regularized solutions, corresponding to the green circle in the trade-off plot, and over-regularized solutions, corresponding to black circle, are also given. Each row in Fig. 9 corresponds to the use of a different regularization penalty functional. In all of these reconstructions, we have imposed that the surface

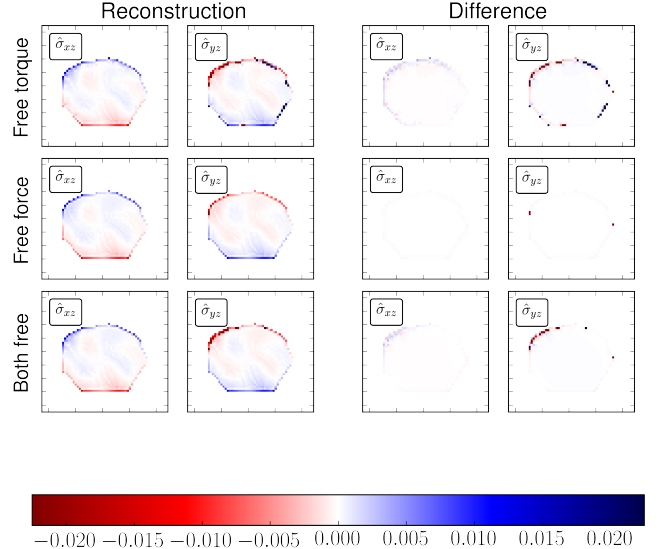


FIG. 6. **Omission of constraints** leads to solutions that do not naturally obey the constraints. Plotted are best reconstructions under the isotropic L^1 penalty and the difference between these reconstructions and the corresponding fully constrained reconstruction of Fig. 9.

stress is both force-free and torque free, and also that the support of the stress is within given cell boundaries.

To explore the effect of the constraints on our reconstructions, we systematically removed them in solving the rotationally invariant L^1 regularized problem. In Fig. 4, we present reconstructions where net torque is free to vary but force is constrained, where net force is free to vary but torque is constrained, and where net torque and force are both free to vary. In each of these reconstructions the unconstrained quantity did not sum to zero, as desired.

Additionally, our reconstructions are implicitly constrained by the assumption of compact support where the support of the stress tensor is within the cell boundary. Examining Fig. 9, it appears that this constraint is active as much of the stress is concentrated at boundaries. In Fig. 5, we loosened the boundary constraint by allowing the support of the stress to fall within 10 pixels of the cell boundary.

RECONSTRUCTION OF STRESS FIELDS FROM DISPLACEMENTS GENERATED BY OSTEOCYTES(?)

Next, we consider experimental displacements resulting from stress generated by a single cell. The surface displacements were measured using Hilbert space dynamometry which uses phase information of the periodic signal arising from a chemically patterned grid on the substrate [13]. Both x and y -displacements at a resolu-

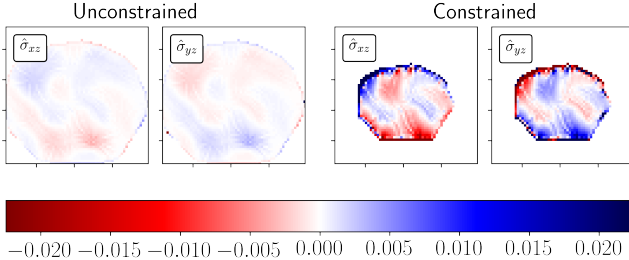


FIG. 7. **Boundary constraint weakening** leads to solutions where the support does not fall naturally within the cell boundary. In the unconstrained reconstruction, the support of the stress was allowed to extend an additional 10 pixels outside of the cell boundary. The reconstruction did not naturally limit its support to the cell boundary.

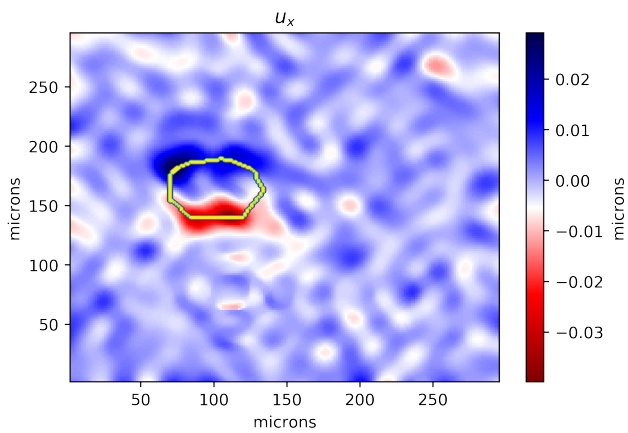


FIG. 8. **Bright field image and displacements.** (a) Raw bright field image of a mesenchymal stem cell. The cell footprint boundary is estimated from segmentation. (b) and (c) The x - and y -displacement fields at the surface of the substrate.

tion of the patterned grid spacing can be measured, as shown in Fig. 8

The results of reconstruction of the stress field using our method are shown in Fig. 9.

DISCUSSION AND CONCLUSIONS

We have presented a comprehensive method for solving the inverse problem of surface stress reconstruction that incorporates physical knowledge as constraints. Under piecewise affine approximations of the stress tensor, we provided an exact solution to the forward problem as a system of linear equations. Using the multipole expansion, we motivated the use of a cut-off in the solution of the forward problem that greatly reduces the rank of the inverse problem thereby decreasing both the computational complexity of the problem and the memory re-

quirements. The numerical stability of the problem was also improved using regularization which obeys the geometric constraint that the problem should be rotationally invariant.

Our method exploits physical constraints that allows for superior reconstruction of complex surface stress fields. We also showed how the known footprint boundary can impact the reconstruction. In general, footprints that extend beyond the extent of the support of the stress field worsens the inversion, allowing for “leakage” of stress beyond its actual support. Our method can naturally apply to related systems such as scratch wound assays.

DISCUSS HOW E , ν , AND THE CELL BOUNDARY CAN ALSO BE SIMULTANEOUSLY INFERRED

-
- [1] M. Prager-Khoutorsky, A. Lichtenstein, R. Krishnan, K. Rajendran, A. Mayo, Z. Kam, B. Geiger, and A. D. Bershadsky, *Nature Cell Biology* **13**, 1457 (2011).
 - [2] T. Pieters and F. van Roy, *Journal of Cell Science* **127**, 2603 (2014).
 - [3] A. Aman and T. Piotrowski, *Developmental Biology* **341**, 20 (2010).
 - [4] L. Schneider, M. Cammer, J. Lehman, S. K. Nielsen, C. F. Guerra, I. R. Veland, C. Stock, E. K. Hoffmann, B. K. Yoder, A. Schwab, P. Satir, and S. T. Christensen, *Cell Physiology and Biochemistry* **25**, 279 (2010).
 - [5] L. Li, Y. He, M. Zhao, and J. Jiang, *Burns and Trauma* **1**, 21 (2013).
 - [6] M. Aragona, S. Dekoninck, S. Rulands, S. Lenglez, G. Mascré, B. D. Simons, and C. Blanpain, *Nature Communications* **8**, 14684 (2017).
 - [7] A. G. Clark and D. M. Vignjevic, *Current Opinion in Cell Biology* **36**, 13 (2015).
 - [8] J. Watson, B. Alberts, D. Bray, M. Raff, and J. Lewis, “Molecular biology of the cell, 6th edition,” (Garland Science, 2014).
 - [9] J. L. Tan, J. Tien, D. M. Pirone, D. S. Gray, K. Bhadriraju, and C. S. Chen, *Proceedings of The National Academy of Sciences USA* **100**, 1484 (2003).
 - [10] N. Q. Balaban, U. S. Schwarz, D. Riveline, P. Goichberg, G. Tzur, I. Sabanay, D. Mahalu, S. Safran, A. Bershadsky, L. Addadi, and B. Geiger, *Nature Cell Biology* **3**, 466 (2001).
 - [11] J. H.-C. Wang and J.-S. Lin, *Biomechanics and Modeling in Mechanobiology* **6**, 361 (2007).
 - [12] B. Sabass, M. L. Gardel, C. M. Waterman, and U. S. Schwarz, *Biophysical Journal* **94**, 207 (2008).
 - [13] S. Sridharana, Y. Li, L. Foucarde, H. Majeed, B. Bhaduria, A. J. Levine, K. Kilian, and G. Popescu, *Nature Methods* (2017).
 - [14] T. Goldstein and S. Osher, *SIAM J. Imaging Sciences* **2**, 323 (2009).
 - [15] T. F. Chan and S. Esedoglu, *SIAM J. Appl. Math.* **65**,

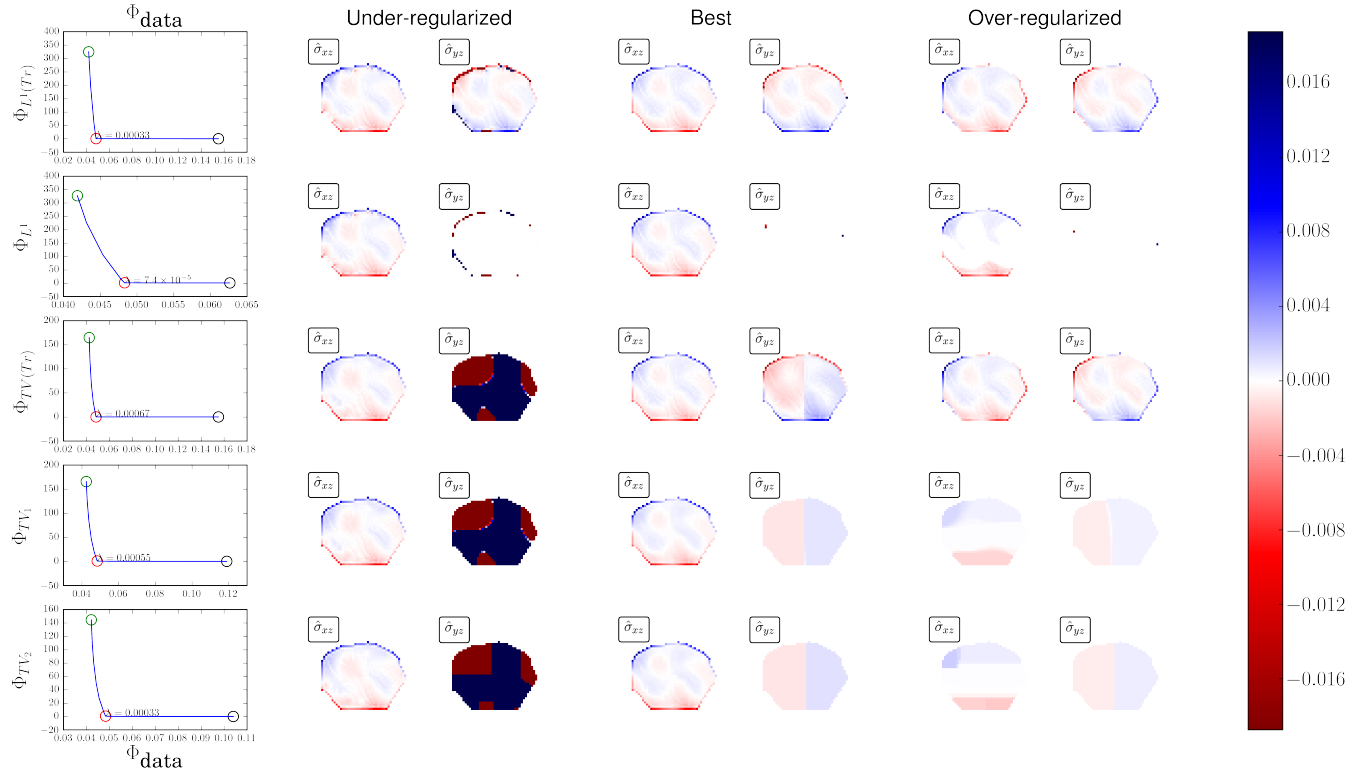


FIG. 9. **Reconstruction of experimental surface stress field** for various choices of regularization. The first and third rows are physically-consistent regularizations. The best reconstruction balances regularity and data matching and corresponds to the value for λ that is near a phase transition in the trade off plot between these two penalties (circled in red). The under-regularized solution corresponds to the point circled in green and the over-regulated solution corresponds to the point circled in black.

- 1817 (2004).
- [16] S. S. Soofia, J. A. Lasta, S. J. Liliensieka, P. F. Nealey, and C. J. Murphy, *Journal of Structural Biology* **167**, 216 (2009).
 - [17] S. Diamond and S. Boyd, *Journal of Machine Learning Research* **17**, 1 (2016).
 - [18] L. D. Landau and E. M. Lifshitz, *Theory of Elasticity* (Pergamon Press, Oxford, 1970).

Appendix A: Elastic Green's function

For completeness, we explicitly list the components of the Green's tensor for a linear elastic substrate [18]

$$G_{ss}(x, y, z) = \frac{1+\nu}{2\pi E} \left[\frac{2(1-\nu)R_\perp - z}{R_\perp(R_\perp - z)} + \frac{[2R_\perp(\nu R_\perp - z) + z^2]s^2}{R_\perp^3(R_\perp - z)^2} \right], \quad (23)$$

$$G_{zz}(x, y, z) = \frac{1+\nu}{2\pi E} \left(\frac{2(1-\nu)}{R_\perp} + \frac{z^2}{R_\perp^3} \right), \quad (24)$$

$$G_{xy}(x, y, z) = G_{yx} = \frac{1+\nu}{2\pi E} \frac{[2R_\perp(\nu R_\perp - z) + z^2]xy}{R_\perp^3(R_\perp - z)^2}, \quad (25)$$

$$G_{sz,zs}(x, y, z) = \frac{1+\nu}{2\pi E} \left(\frac{sz}{R_\perp^3} \pm \frac{(1-2\nu)s}{R_\perp(R_\perp - z)} \right). \quad (26)$$

where $s \equiv x, y$. The last equation with \pm corresponds to G_{sz} and G_{zs} , respectively, and $R_\perp \equiv \sqrt{x^2 + y^2}$. The Young's modulus and Poisson ratio of the elastic substrate are denoted by E and ν , respectively.

Appendix B: Displacements and stresses at discrete positions

Here, we show the explicit expressions relating displacements $\mathbf{u}(x_n, y_m)$ at grid points (x_n, y_m) in terms of stress fields at the same locations. Using the interpolation of $\sigma(x, y)$ defined by Eq. 5 in Eq. 3, we find

$$\begin{aligned} u_x(x_n, y_m) = & \sum_{(x_j, y_k) \in \Omega} \left\{ \left[\sigma_{xz}(x_j, y_k) - x_j \left(\frac{\sigma_{xz}(x_{j+1}, y_k) - \sigma_{xz}(x_{j-1}, y_k)}{2\delta x} \right) - y_k \left(\frac{\sigma_{xz}(x_j, y_{k+1}) - \sigma_{xz}(x_j, y_{k-1})}{2\delta y} \right) \right] \langle G_{xx} \rangle^{nmjk} \right. \\ & + \left[\frac{\sigma_{xz}(x_{j+1}, y_k) - \sigma_{xz}(x_{j-1}, y_k)}{2\delta x} \right] \langle xG_{xx} \rangle^{nmjk} + \left[\frac{\sigma_{xz}(x_j, y_{k+1}) - \sigma_{xz}(x_j, y_{k-1})}{2\delta y} \right] \langle yG_{xx} \rangle^{nmjk} \\ & + \left[\sigma_{yz}(x_j, y_k) - x_j \left(\frac{\sigma_{yz}(x_{j+1}, y_k) - \sigma_{yz}(x_{j-1}, y_k)}{2\delta x} \right) - y_k \left(\frac{\sigma_{yz}(x_j, y_{k+1}) - \sigma_{yz}(x_j, y_{k-1})}{2\delta y} \right) \right] \langle G_{xy} \rangle^{nmjk} \\ & \left. + \left[\frac{\sigma_{yz}(x_{j+1}, y_k) - \sigma_{yz}(x_{j-1}, y_k)}{2\delta x} \right] \langle xG_{xy} \rangle^{nmjk} + \left[\frac{\sigma_{yz}(x_j, y_{k+1}) - \sigma_{yz}(x_j, y_{k-1})}{2\delta y} \right] \langle yG_{xy} \rangle^{nmjk} \right\}, \end{aligned} \quad (27)$$

where

$$\langle g(x, y)G_{uv} \rangle^{nmjk} = \int_{y_k - \delta y/2}^{y_k + \delta y/2} \int_{x_j - \delta x/2}^{x_j + \delta x/2} g(x', y') G_{uv}(x_n - x', y_m - y') dx' dy', \quad (28)$$

except that at the edges where we use one-sided differences so that we are only differentiating within Ω . A similar expression can be found for solving for u_y (not shown). Collecting terms, we write $u_{x,y}(x_n, y_m)$ in terms of $\sigma(x_j, y_k)$ in Eq. 6, where

$$\begin{aligned} X^{nmjk} = & \langle G_{xx} \rangle^{nmjk} - \langle G_{xx} \rangle^{n,m,j-1,k} \frac{x_{j-1}}{2\delta x} + \langle G_{xx} \rangle^{n,m,j+1,k} \frac{x_{j+1}}{2\delta x} - \langle G_{xx} \rangle^{n,m,j,k-1} \frac{y_{k-1}}{2\delta y} \\ & + \langle G_{xx} \rangle^{n,m,j,k+1} \frac{y_{k+1}}{2\delta y} - \frac{\langle xG_{xx} \rangle^{n,m,j-1,k}}{2\delta x} + \frac{\langle xG_{xx} \rangle^{n,m,j+1,k}}{2\delta x} - \frac{\langle yG_{xx} \rangle^{n,m,j,k-1}}{2\delta y} + \frac{\langle yG_{xx} \rangle^{n,m,j,k+1}}{2\delta y}, \end{aligned} \quad (29)$$

$$Y^{nmjk} = \langle G_{xy} \rangle^{nmjk} - \langle G_{xy} \rangle^{n,m,j-1,k} \frac{x_{j-1}}{2\delta x} + \langle G_{xy} \rangle^{n,m,j+1,k} \frac{x_{j+1}}{2\delta x} - \langle G_{xy} \rangle^{n,m,j,k-1} \frac{y_{k-1}}{2\delta y} \\ + \langle G_{xy} \rangle^{n,m,j,k+1} \frac{y_{k+1}}{2\delta y} - \frac{\langle xG_{xy} \rangle^{n,m,j-1,k}}{2\delta x} + \frac{\langle xG_{xy} \rangle^{n,m,j+1,k}}{2\delta x} - \frac{\langle yG_{xy} \rangle^{n,m,j,k-1}}{2\delta y} + \frac{\langle yG_{xy} \rangle^{n,m,j,k+1}}{2\delta y}. \quad (30)$$

Explicit closed-form expressions for the integrals in Eq. 28 are given below. By defining $\Delta x_{nj}^+ = x_n - (x_j + \delta x/2)$, $\Delta x_{nj}^- = x_n - (x_j - \delta x/2)$, $\Delta y_{mk}^+ = y_m - (y_k + \delta y/2)$, and $\Delta y_{mk}^- = y_m - (y_k - \delta y/2)$, we find

$$\langle G_{uv} \rangle^{nmjk} = f_{uv}(\Delta x_{nj}^+, \Delta y_{mk}^+) - f_{uv}(\Delta x_{nj}^+, \Delta y_{mk}^-) - f_{uv}(\Delta x_{nj}^-, \Delta y_{mk}^+) + f_{uv}(\Delta x_{nj}^-, \Delta y_{mk}^-) \quad (31)$$

where

$$f_{xx}(x, y) = \frac{\nu + 1}{\pi E} \left[x(1 - \nu) \log \left(\sqrt{x^2 + y^2} + y \right) + y \log \left(\sqrt{x^2 + y^2} + x \right) - y \right] \quad (32)$$

$$f_{yy}(x, y) = \frac{\nu + 1}{\pi E} \left[y(1 - \nu) \log \left(\sqrt{x^2 + y^2} + x \right) + x \log \left(\sqrt{x^2 + y^2} + y \right) - x \right] \quad (33)$$

$$f_{xy}(x, y) = -\frac{\nu(\nu + 1)}{\pi E} \sqrt{x^2 + y^2}. \quad (34)$$

The first moments are

$$\langle xG_{xx}(x, y) \rangle^{nmjk} = \left[f_{xx}(\Delta x_{nj}^+, \Delta y_{mk}^+) - f_{xx}(\Delta x_{nj}^+, \Delta y_{mk}^-) - f_{xx}(\Delta x_{nj}^-, \Delta y_{mk}^+) + f_{xx}(\Delta x_{nj}^-, \Delta y_{mk}^-) \right] x_n \\ - \left[f_{xx}^x(\Delta x_{nj}^+, \Delta y_{mk}^+) - f_{xx}^x(\Delta x_{nj}^+, \Delta y_{mk}^-) - f_{xx}^x(\Delta x_{nj}^-, \Delta y_{mk}^+) + f_{xx}^x(\Delta x_{nj}^-, \Delta y_{mk}^-) \right], \quad (35)$$

where

$$f_{xx}^x(x, y) = \frac{\nu + 1}{2\pi E} \left[(\nu + 1)y\sqrt{x^2 + y^2} - (\nu - 1)x^2 \log \left(\sqrt{x^2 + y^2} + y \right) \right], \quad (36)$$

$$\langle yG_{xx}(x, y) \rangle^{nmjk} = \left[f_{xx}(\Delta x_{nj}^+, \Delta y_{mk}^+) - f_{xx}(\Delta x_{nj}^+, \Delta y_{mk}^-) - f_{xx}(\Delta x_{nj}^-, \Delta y_{mk}^+) + f_{xx}(\Delta x_{nj}^-, \Delta y_{mk}^-) \right] y_m \\ - \left[f_{xx}^y(\Delta x_{nj}^+, \Delta y_{mk}^+) - f_{xx}^y(\Delta x_{nj}^+, \Delta y_{mk}^-) - f_{xx}^y(\Delta x_{nj}^-, \Delta y_{mk}^+) + f_{xx}^y(\Delta x_{nj}^-, \Delta y_{mk}^-) \right], \quad (37)$$

where

$$f_{xx}^y(x, y) = \frac{\nu + 1}{2\pi E} \left[y^2 \log \left(\sqrt{x^2 + y^2} + x \right) - \sqrt{x^2 + y^2} \left((2\nu - 1)x + \frac{1}{2}\sqrt{x^2 + y^2} \right) \right], \quad (38)$$

and

$$\langle xG_{xy}(x, y) \rangle^{nmjk} = \left[f_{xy}(\Delta x_{nj}^-, \Delta y_{mk}^+) - f_{xy}(\Delta x_{nj}^-, \Delta y_{mk}^-) - f_{xy}(\Delta x_{nj}^+, \Delta y_{mk}^+) + f_{xy}(\Delta x_{nj}^+, \Delta y_{mk}^-) \right] x_n \\ - \left[f_{xy}^x(\Delta x_{nj}^+, \Delta y_{mk}^+) - f_{xy}^x(\Delta x_{nj}^+, \Delta y_{mk}^-) - f_{xy}^x(\Delta x_{nj}^-, \Delta y_{mk}^+) + f_{xy}^x(\Delta x_{nj}^-, \Delta y_{mk}^-) \right] \quad (39)$$

where

$$f_{xy}^x(x, y) = \frac{\nu(\nu + 1)}{\pi E} \left[\frac{y^2}{2} \log \left(\sqrt{x^2 + y^2} + x \right) - \frac{1}{4}\sqrt{x^2 + y^2} \left(\sqrt{x^2 + y^2} + 2x \right) \right]. \quad (40)$$

All of these expressions may be found through direct iterated evaluation of the integrals, noting that as long as $n \neq m$ or $j \neq k$ the integrand (effectively the Green's function) is bounded, hence making Fubini's theorem applicable given the compactly supported domains of integration.

In the special case where $n = m$ and $j = k$, these formulae also hold. This fact is found by decomposing the integration domain to exclude the origin, for instance in the manner

$$\int_{-\Delta y/2}^{\Delta y/2} \int_{-\Delta x/2}^{\Delta x/2} d\mathbf{r} = \lim_{\varepsilon \rightarrow 0} \left(\int_{\varepsilon}^{\Delta y/2} + \int_{-\Delta y/2}^{-\varepsilon} \right) \int_{\Delta x/2}^{\Delta x/2} d\mathbf{r}. \quad (41)$$

Since the antiderivatives of Eqs 32, 33, 34, 36, 38, and 40 all have well-defined limits with only removable discontinuities at the origin, integrals of the Green's functions defined through Eq. 41 all converge about the origin and the equations above also hold in the case where $n = m$ and $j = k$. These explicit expressions allow us to accurately evaluate $\mathbf{u}(\mathbf{r}_i)$ in $\Phi_{\text{data}}[\boldsymbol{\sigma}]$.

Appendix C: Decay of displacement fields

Note that u_x and u_y are symmetric in form. Hence, it will suffice to prove just one of these assertions. Eq. 3 can be written as

$$\begin{aligned} u_x(\mathbf{r}) &= \frac{1+\nu}{\pi E} \int \frac{d\mathbf{r}}{|\mathbf{r}-\mathbf{r}'|} \left\{ \left[\frac{\nu(x-x')^2}{|\mathbf{r}-\mathbf{r}'|^2} + 1 - \nu \right] \sigma_x(\mathbf{r}') + \nu \frac{(x-x')(y-y')}{|\mathbf{r}-\mathbf{r}'|^2} \sigma_y(\mathbf{r}') \right\} \\ &\equiv \frac{1+\nu}{\pi E} \int \frac{\rho_x(\mathbf{r}, \mathbf{r}')}{|\mathbf{r}-\mathbf{r}'|} d\mathbf{r}' \end{aligned} \quad (42)$$

where $\rho_x(\mathbf{r}, \mathbf{r}')$ is $\mathcal{O}(1)$ as $|\mathbf{r}| \rightarrow \infty$. Without loss of generality, we assume that the coordinate system is centered at some point $\mathbf{0} \in \Omega$. The Euclidean distances can then be represented through the binomial expansion,

$$\frac{1}{|\mathbf{r}-\mathbf{r}'|^p} = \frac{1}{|\mathbf{r}|^p} \frac{1}{\left(1 - \frac{2\mathbf{r} \cdot \mathbf{r}'}{|\mathbf{r}|^2} + \frac{|\mathbf{r}'|^2}{|\mathbf{r}|^2}\right)^{p/2}} = \frac{1}{|\mathbf{r}|^p} \sum_{k=0}^{\infty} \binom{\frac{p}{2} + k - 1}{k} \underbrace{\left(\frac{2\mathbf{r} \cdot \mathbf{r}' - |\mathbf{r}'|^2}{|\mathbf{r}|^2} \right)}_{\mathcal{O}(|\mathbf{r}|^{-1})}^k. \quad (43)$$

Since $\mathbf{r} \notin \Omega$ and $\mathbf{r}' \in \Omega$, the series converges in the $|\mathbf{r}| \rightarrow \infty$ limit. Plugging this series into the last line of Eq. 42, where $p = 1$, one sees that it in order to show that the magnitude of $u_x(\mathbf{r})$ is $\mathcal{O}(|\mathbf{r}|^{-q})$, it suffices to show that $\int \rho(\mathbf{r}, \mathbf{r}') d\mathbf{r}' \leq \mathcal{O}(|\mathbf{r}|^{-q+1})$.

Using the fact that $\int \boldsymbol{\sigma}(\mathbf{r}) d\mathbf{r} = \mathbf{0}$, one finds that

$$\begin{aligned} \int \rho_x(\mathbf{r}, \mathbf{r}') d\mathbf{r}' &= \int (1-\nu) \sigma_x(\mathbf{r}') d\mathbf{r}' + \nu \int \left[\frac{(x-x')^2}{|\mathbf{r}-\mathbf{r}'|^2} \sigma_x(\mathbf{r}') + \frac{(x-x')(y-y')}{|\mathbf{r}-\mathbf{r}'|^2} \sigma_y(\mathbf{r}') \right] d\mathbf{r}' \\ &= \frac{\nu}{|\mathbf{r}|^2} \int \left[(x-x')^2 \sigma_x(\mathbf{r}') + (x-x')(y-y') \sigma_y(\mathbf{r}') \right] \sum_{k=0}^{\infty} \left[\frac{2\mathbf{r} \cdot \mathbf{r}' - |\mathbf{r}'|^2}{|\mathbf{r}|^2} \right]^k d\mathbf{r}'. \end{aligned} \quad (44)$$

Expanding the leading order term of this expression, we see that

$$\begin{aligned} \int \rho_x(\mathbf{r}, \mathbf{r}') d\mathbf{r}' &= \frac{\nu}{|\mathbf{r}|^2} \int \left[(x-x')^2 \sigma_x(\mathbf{r}') + (x-x')(y-y') \sigma_y(\mathbf{r}') \right] d\mathbf{r}' \\ &= \frac{\nu}{|\mathbf{r}|^2} \left[-2x \int x' \sigma_x(\mathbf{r}') d\mathbf{r}' + \int x'^2 \sigma_x(\mathbf{r}') d\mathbf{r}' - x \int y' \sigma_y(\mathbf{r}') d\mathbf{r}' - y \int x' \sigma_y(\mathbf{r}') d\mathbf{r}' + \int x' y' \sigma_y(\mathbf{r}') d\mathbf{r}' \right] \\ &= \mathcal{O}(|\mathbf{r}|^{-1}). \end{aligned}$$

Hence, it is evident that this integral of $\mathcal{O}(|\mathbf{r}|^{-2})$, where to the leading order we have

$$u_x(\mathbf{r}) = \frac{1+\nu}{\pi E |\mathbf{r}|^2} \left[-2\nu \frac{x}{|\mathbf{r}|} \int x' \sigma_x(\mathbf{r}') d\mathbf{r}' - \frac{x\nu}{|\mathbf{r}|} \int y' \sigma_y(\mathbf{r}') d\mathbf{r}' \right. \\ \left. - \frac{y\nu}{|\mathbf{r}|} \int x' \sigma_y(\mathbf{r}') d\mathbf{r}' + (1-\nu) \frac{\mathbf{r}}{|\mathbf{r}|} \cdot \int \mathbf{r}' \sigma_x(\mathbf{r}') d\mathbf{r}' \right] + \mathcal{O}(|\mathbf{r}|^{-3}) \quad (45)$$
